Experimental Study on the Methane Adsorption of Massive Shale Considering the Effective Stress and the Participation of Nanopores of Varying Sizes

Feng Miao, Di Wu,* Nan Jia, Xiaochun Xiao, Weiji Sun, Xin Ding, Wenbo Zhai, and Xintong Chen

ACCESS | 📊 Metrics & More | 📖 Article Recommendations

ABSTRACT: To explore the shale gas occurrence mechanism in shale with an intact pore structure under actual reservoir conditions, an adsorption experiment on massive shale was performed. Considering the change in the pore volume of massive shale under effective stress, the adsorption mechanism and free gas storage space of massive shale were investigated. Based on the adsorption mechanism assumptions of micropore filling and mesopore multilayer adsorption, the adsorbed phase densities of pores of varying pore sizes were calculated and applied to the conversion of the absolute adsorption amount of massive shale. The results show the existence of isolated pores in the massive shale, resulting in a lower adsorption capacity in comparison to granular samples. When subjected to the combined effects of in situ stress and pore pressure, the pore volume of massive shale gradually decreases with the increase in effective stress. Shale gas is mainly adsorbed in micropores, but with increasing pressure, the adsorption amount of micropores approaches saturation, and the contribution of mesopores to the total adsorption amount gradually increases. The main adsorption mechanism of shale gas is based on micropore filling, and the multilayer surface adsorption of mesopores should also be considered. By combining the simplified local density model and the Ono−Kondo lattice model, the adsorption behavior of shale gas can be accurately described. To accurately estimate shale gas reserves, it is necessary to take into account the actual pore size distribution, pore volume compressibility, and connected porosity of the shale samples.
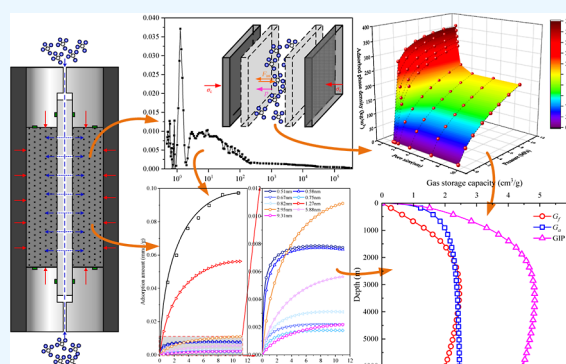
1. INTRODUCTION

Shale gas, with its wide distribution and large reserves,[1] is bound to play an important role in the transition from traditional fossil energy to renewable energy.[2] In recent years, the shale gas revolution has been underway around the world.[3−5] Accurate evaluation of shale gas reserves is a prerequisite for shale gas development.[6] However, current research on shale gas content is mostly based on the experimental results of granular samples under unconstrained conditions, which cannot simulate the changes in shale pore characteristics under the combined action of high in situ stress and high pore pressure in deep shale reservoirs.[7] Therefore, it is of great significance to study shale gas content under effective stress based on the pore pressure gradient for the accurate evaluation of shale gas content.

Shale gas occurs in shale gas reservoirs in mostly adsorbed and free states, with a lesser amount in the dissolved state. Adsorption is one of the main mechanisms of shale gas occurrence,[8] and the adsorbed gas content accounts for approximately 20−85% of the shale gas content.[9] Therefore, the evaluation of the adsorbed gas content in shale is particularly important. In recent years, many scholars have used adsorption experiments based on the volumetric method or gravimetric method to investigate how the adsorption capacity of shale is affected by its mineral composition, pore structure, and organic carbon content under different reservoir conditions (pressure, temperature, water content, etc.)[10−17] Some scholars have also proposed adsorption mechanism assumptions, such as pore filling and multilayer adsorption,[18−20] and established corresponding adsorption models based on the assumptions, such as the Langmuir, supercritical Dubinin−Radushkevich (SDR), simplified local density (SLD), and Ono−Kondo lattice (OK) models,[21−28] to describe the gas adsorption behavior in shale. Grand canonical Monte Carlo and molecular dynamics simulation approaches also have been used to investigate the adsorption behavior of different minerals in shale,[10,29−31] which further improves our understanding of the adsorption mechanism of gas in shale.

Most of the above research results are based on artificially created granular shale samples with pore structures that are different from the original pore structure of a shale in situ. Due to the increased specific surface area (SSA), the adsorption capacity of these shale samples is overestimated.[32] In addition, the free gas in shale reservoirs is an important part of shale gas, and the evaluation of free gas content in shale reservoirs mainly depends on the effective pore volume.[33,34] In deep shale reservoirs, the combined action of high in situ stress and high pore pressure leads to the deformation of shale pore volume, and the adsorbed phase formed by adsorption occupies a certain pore volume, leading to a change in the effective pore volume of the shale.[34,35] However, it is difficult to apply an external force to simulate the effect of effective stress on granular samples. In summary, there are many limitations in the study of shale gas content with granular specimens. In recent years, to further understand the occurrence mechanism of gas in shale, Kang et al.[36] and Santos and Akkutlu[37] studied the gas storage ability of massive shale under constrained conditions and found that both the pore volume compressibility and the adsorption effect of different pore sizes would affect the gas storage ability of shale.

In this study, a CH_4 adsorption experiment at a temperature of 308.15 K, confining pressure of 20 MPa, and gas pressure of up to 15 MPa was conducted on a massive shale sample with a custom-made massive shale adsorption experimental setup. Considering the influence of the pore volume of the massive shale sample under effective stress, the CH_4 adsorption isotherm of the massive shale was calculated. According to the full-size pore size distribution (PSD) of the shale sample, the contributions of pores with varying pore sizes in shale to adsorption were studied by the SLD model. Based on the adsorption mechanism assumptions of micropore filling and mesopore multilayer adsorption, the adsorbed phase densities in micropores and mesopores were calculated by the SLD model and the OK model, respectively. Then, considering the contribution of pores with varying pore sizes, the excess adsorption amount of massive shale was converted into the absolute adsorption amount according to the adsorbed phase densities of the corresponding pores. Finally, the gas in place (GIP) of the massive shale sample was estimated by taking into account the PSD, pore volume compressibility, and connected porosity. This study preliminarily explored the occurrence mechanism of shale gas at the core scale and proposed a method for the conversion of the absolute adsorption amount of massive shale. These findings can further improve the accuracy of shale gas evaluation.

2. MATERIALS AND METHODS

2.1. Shale Sample Collection. In this study, a shale outcrop sample from the Silurian Longmaxi shale formation was collected to perform basic petrophysical tests, as shown in Table 1.

**Table 1. Basic Petrophysical Properties of the Shale Sample**

TOC (%)	porosity (%)	pore volume ×10^{-3} (cm³/g)	bulk density (g/cm³)	grain density (g/cm³)
1.87	6.12	24.58	2.49	2.65
X-ray diffraction mineralogical composition (%)				
quartz	calcite	dolomite	total clay	pyrite	plagioclase	potash feldspar
43.7	20.2	14.3	12.4	5.1	3.1	1.2

2.2. Pore Structure Characterization Tests. In this study, low-pressure CO_2 adsorption (LP-CO_2-GA), low-pressure N_2 adsorption (LP-N_2-GA), and mercury intrusion porosimetry (MIP) were used to characterize the PSD, SSA, and total pore volume (TPV) of micropores, mesopores, and macropores. LP-CO_2-GA and LP-N_2-GA were performed with an ASAP 2020 system, and MIP was performed with an AutoPore IV 9500. Nonlocalized density functional theory was applied to characterize the PSD, SSA, and TPV of the shale sample. Finally, the pore structure characterization results of micropores, mesopores, and macropores were combined to obtain the full-size pore structure of the shale sample.

2.3. Experimental System and Procedure. *2.3.1. Massive Shale Adsorption Experimental System.* In view of the existing research requirements, the following requirements are proposed for the "massive shale adsorption experimental setup" that can measure the change in pore volume of samples under effective stress:

- Massive samples can be subjected to volumetric stress.
- The change in the pore volume of a sample under effective stress can be measured.
- The free space volume of the sample cell can be minimized as much as possible.
- The contact area between the gas and the test piece increases during the test.

Based on the above requirements, the experimental method of the adsorption experiment was first selected, which was divided into the gravimetric method and volumetric method. The gravimetric method is a method of measuring the increased weight of adsorbed gas with a high-precision balance. Due to the scale problem of the balance, the gravimetric method cannot include the core holding device. The volumetric method is a method of measuring the adsorption amount by measuring the amount of gas before and after adsorption. The corresponding experimental principle and device are simple and scalable. Therefore, the experimental setup is designed based on the volumetric method. The core component of the volumetric method consists of a sample cell and a reference cell. To apply volumetric stress to the sample, a triaxial core holding device was selected as the sample cell. Because the unbroken massive shale is dense, the contact area between the gas and the shale is small at the beginning of the experiment, and the gas needs to diffuse into the sample before being adsorbed, which leads to a long adsorption saturation time.[38] To shorten the adsorption saturation time, the core holding device was improved. Under the premise of massive shale, a gas pipe was added to the axis of the core holding device to increase the contact area between the gas and the sample. The improved holding setup and the prepared massive shale sample are shown in Figure 1a. In the process of the adsorption experiment, the change in the pore volume of the massive shale under the effective stress of the pore pressure gradient is not negligible. Before the adsorption experiment, it is necessary to measure the change rule of the pore volume of the sample. Therefore, two reference cells were designed to store the adsorbed gas and free space measurement gas (He). As suggested by Mohammad et al.,[39] to improve the measurement accuracy, the ratio of the sample cell volume to the reference cell volume should be at least 2.0. However, the volume of the sample cell in this experimental setup is controlled by the pore volume of the sample and is not a fixed value. The volume of the reference cell needs to be determined after the start of the experiment. In this setup, the volume of the reference
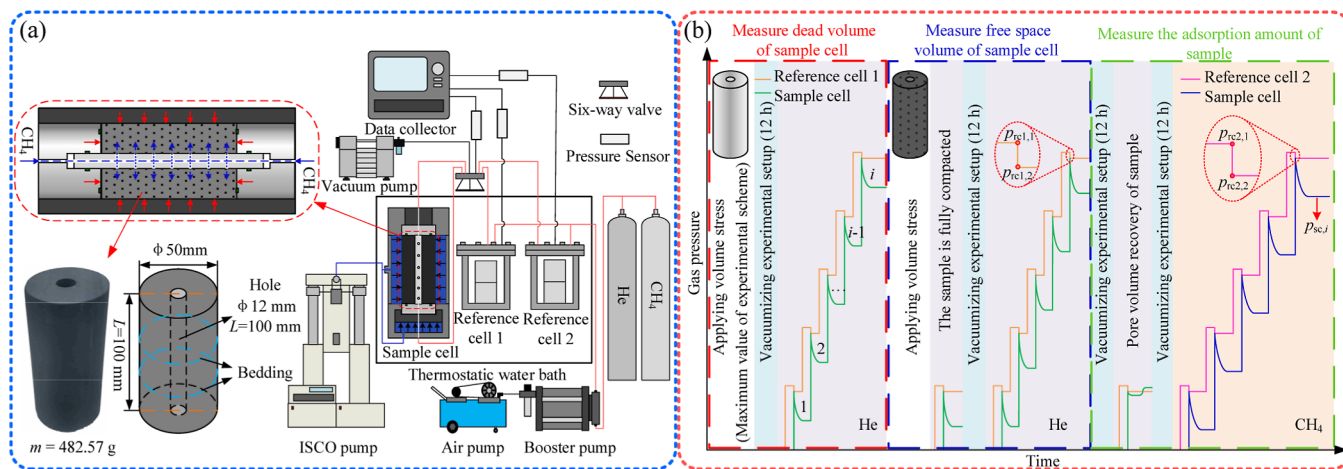
Figure 1. Schematic diagram of the experimental system and experimental process. (a) Massive shale adsorption experimental system and massive shale sample and (b) experimental procedure of massive shale adsorption.

cell was changed by adding/reducing the standard volume block to/from the reference cell. The experimental setup is shown in Figure 1a, and the remaining devices in the figure are all required for the conventional volumetric method.

2.3.2. Experimental Procedure. The experimental procedure is mainly divided into three parts: measuring the dead volume of the sample cell, measuring the free volume of the sample cell containing the shale sample, and measuring the adsorption capacity of the bulk sample. First, the dead volume of the sample cell was measured at helium pressures up to 13 MPa and a constant confining pressure (20 MPa) using a stainless-steel sample. A total of seven measurements were made as the helium pressure was increased, and the gas pressure was stabilized for 1 h each time. Then, the free volume of the sample cell was measured at pore pressures up to 20 MPa and different confining pressures (20, 30, and 40 MPa) using the massive shale sample. With increasing helium pressure, a total of six measurements were taken, and a change in sample cell pressure of less than 0.002 MPa within 24 h was used as the criterion for judging whether an equilibrium was reached. The equilibration time after the initial gas injection was approximately 13 days, after which the time required for equilibration was reduced to 10 to 6 days as the gas pressure increased. Finally, the adsorption experiment was carried out with the massive shale sample under a constant confining pressure (20 MPa) and CH_4 pressures up to 15 MPa. Similarly, the change in pressure of the sample cell within 24 h was less than 0.002 MPa as the adsorption reached equilibrium, and the adsorption equilibrium time ranged from 7 to 15 days. The above experiments were carried out at a constant temperature of 308.15 K, and the specific experimental process is shown in Figure 1b.

2.3.3. Calculation Procedure of Experimental Results. 2.3.3.1. Sample Pore Volume Calculation Procedure. The free volumes of the sample cell containing the rust-free steel sample and the shale sample are calculated by the following eq 1, and the difference between the two can be used to obtain the pore volumes of the shale sample at different gas pressures.

$$V_{sc,i} = \frac{n_{inj,i}^{H_2} Z_{sc,i}^{H_2} RT}{p_{sc,i}^{H_2}} \tag{1}$$

where

$$n_{inj,i}^{H_2} = \frac{V_{rc1}}{RT}\left(\frac{p_{rc1,1}}{Z_{rc1,1}} - \frac{p_{rc1,2}}{Z_{rc1,2}}\right) + n_{inj,i-1}^{H_2} \tag{2}$$

where $V_{sc,i}$ is the volume including the sample cell, pipeline, and pore volume of the sample; $n_{inj,i}^{H_2}$ is the molar amount of helium (H_e) injected into the sample cell; $Z_{sc,i}^{H_2}$ is the compressibility factor of H_2; $p_{sc,i}^{H_2}$ is the pressure of H_2; R is the universal gas constant; T is the absolute temperature; V_{rc1} is the volume of the reference cell no. 1; $p_{re1,1}$ and $p_{re1,2}$ are the gas pressures in the reference cell before and after injection, respectively; $Z_{re1,1}$ and $Z_{re1,2}$ represent the compressibility factor of the corresponding state gas; and the subscript "i" denotes the i-th experimental point.

2.3.3.2. Adsorption Calculation Procedure. The calculation formula for the adsorption amount measured by the isotherm adsorption experiment based on the volumetric method is as follows

$$n_{exp,i} = n_{inj,i} - n_{unads,i} \tag{3}$$

where

$$n_{inj,i} = \frac{V_{rc2}}{RT}\left(\frac{p_{rc2,1}}{Z_{rc2,1}} - \frac{p_{rc2,2}}{Z_{rc2,2}}\right) + n_{inj,i-1} \tag{4}$$

$$n_{unads,i} = \frac{V_{sc}^{p_{sc,i}}}{RT}\left(\frac{p_{sc,i}}{Z_{sc,i}}\right) \tag{5}$$

where $n_{exp,i}$ is the adsorption amount measured by the isotherm adsorption experiment, $n_{inj,i}$ is the molar amount of the gas injected into the sample cell, $n_{unads,i}$ is the molar amount of unadsorbed gas in the sample cell, V_{rc2} is the volume of the reference cell no. 2, $p_{re2,1}$ and $p_{re2,2}$ are the gas pressures in reference cell no. 2 before and after injection, respectively, $Z_{re2,1}$ and $Z_{re2,2}$ respectively represent the compressibility factor of the corresponding state gas, $V_{sc}^{p_{sc,i}}$ is the $V_{sc,i}$ when the gas pressure is $p_{sc,i}$ and $p_{sc,i}$ and $Z_{sc,i}$ are gas pressures in the sample cell and the compressibility factor of the corresponding state gas, respectively. The gas compressibility factors in the above calculation process were obtained from the National Institute for Standards and Technology (NIST) Chemistry Webbook.

2.4. Determination Methods of Adsorbed Phase Density. *2.4.1. Calculation of the Gas Density Distribution in Nanopores Using a Simplified Local Density Model.* In this study, the SLD model was used to calculate the gas density distribution in shale nanopores. This model utilizes a mean-field approach to calculate the gas adsorption in a slit-shaped pore with the consideration of both fluid−solid interaction and fluid−fluid interaction. The premise assumptions and basic equations of the SLD model are described in detail in the literature.[26]

In this study, Lee's partially integrated 10-4 potential model is used to express the fluid−solid interaction (Ψ_{fs})

$$\Psi_{fs}(z) = 4\pi\rho_{atoms}\varepsilon_{fs}\sigma_{fs}^2\left[\frac{1}{5}\left(\frac{\sigma_{fs}}{z + \frac{\sigma_{ss}}{2}}\right)^{10}\right.$$
$$\left. - \frac{1}{2}\sum_{i=1}^{4}\left(\frac{\sigma_{fs}}{z + \frac{\sigma_{ss}}{2} + (i-1)\sigma_{ss}}\right)^4\right] \quad (6)$$

where

$$\varepsilon_{fs} = \sqrt{\varepsilon_{ff} \times \varepsilon_{ss}} \quad (7)$$

$$\sigma_{fs} = \frac{\sigma_{ff} + \sigma_{ss}}{2} \quad (8)$$

where ρ_{atoms} is the density of carbon atoms; ε_{fs} is the fluid−solid interaction energy; ε_{ff} and ε_{ss} are the fluid−fluid interaction energy and solid−solid interaction energy, respectively; σ_{ss} and σ_{ff} are the molecular diameters of the carbon and the adsorbate interplanar distance, respectively; and z is the distance from the pore wall. The values of the above parameters in this study were as follows: $\sigma_{ss} = 0.335$ nm, $\sigma_{ff} = 0.3758$ nm, $\varepsilon_{ss}/k = 25.1$ K, $\varepsilon_{ff}/k = 148.6$ K, and $\rho_{atoms} = 38.2$ nm^{-2}.

The Peng−Robinson equation of state (PR-EOS) was used to determine the bulk phase density, bulk phase fugacity and fluid fugacity. The bulk density is calculated as follows

$$\frac{p}{\rho RT} = \frac{1}{1 - b\rho} - \frac{a(T)\rho}{RT(1 + 2b\rho - b^2\rho^2)} \quad (9)$$

where

$$a(T) = \frac{0.45735\alpha(T)R^2T_c^2}{p_c} \quad (10)$$

$$b = \frac{0.077796RT_c}{p_c} \quad (11)$$

Regarding eq 10, Gasem et al.[40] introduced an expression of term $\alpha(T)$ as follows

$$\alpha(T) = \exp[(2.0 + 0.8145(T/T_c))\cdot$$
$$(1 - (T/T_c)^{0.134+0.508\omega-0.0467\omega^2})] \quad (12)$$

where p_c, T_c, and ω indicate the critical pressure, critical temperature, and acentric factor of the adsorbed gas, respectively (for CH$_4$, $p_c = 4.599$ MPa, $T_c = 190.56$ K, and $\omega = 0.01142$).

Based on eq 9, the bulk phase fluid fugacity and adsorbed phase fluid fugacity can be expressed by PR-EOS as

$$\ln\frac{f_{bulk}}{p} = \frac{b\rho}{1 - b\rho} - \frac{a(T)\rho}{RT(1 + 2b\rho - b^2\rho^2)}$$
$$- \ln\left[\frac{p}{RT\rho} - \frac{pb}{RT}\right]$$
$$- \frac{a(T)}{2\sqrt{2}\,bRT}\ln\left[\frac{1 + (1 + \sqrt{2})b\rho}{1 + (1 - \sqrt{2})b\rho}\right] \quad (13)$$

$$\ln\frac{f_{ff}(z)}{p} = \frac{b_{ads}\rho(z)}{1 - b_{ads}\rho(z)}$$
$$- \frac{a_{ads}(z)\rho(z)}{RT(1 + 2b_{ads}\rho(z) - b_{ads}^2\rho(z)^2)}$$
$$- \ln\left[\frac{p}{RT\rho(z)} - \frac{pb_{ads}}{RT}\right]$$
$$- \frac{a_{ads}(z)}{2\sqrt{2}\,b_{ads}RT}\ln\left[\frac{1 + (1 + \sqrt{2})b_{ads}\rho(z)}{1 + (1 - \sqrt{2})b_{ads}\rho(z)}\right] \quad (14)$$

where $\rho(z)$ is the phase density profile in a slit-shaped pore and $a_{ads}(z)$ is the van der Waals attractive parameter and is calculated from the expressions developed by Chen et al.[41] b_{ads} is the covolume for the adsorbed phase, which can be expressed as $b_{ads} = b(1 + \Lambda_b)$,[41] adjusting Λ_b (ranging from −0.3 to 0.3) to accurately characterize the repulsive interactions of the adsorbed phase at high pressure. Substituting eqs 6, 13, and 14 into the basic equation of the SLD model can provide an expression with which to calculate $\rho(z)$.

2.4.2. Adsorbed Phase Density Calculation. 2.4.2.1. Adsorbed Phase Density Calculation with the Simplified Local Density Model. At present, there are two methods to calculate the adsorbed phase density according to the nanopore size. For micropores and mesopores with smaller sizes, the adsorption mechanism is assumed to be micropore filling. Therefore, the entire pore corresponds to the adsorbed phase, and the adsorbed phase density is the average density within the pore. The adsorbed phase density in SLD theory can be expressed as[42]

$$\rho_a = \frac{1}{L - \frac{3}{4}\sigma_{ff}}\int_{3/8\sigma_{ff}}^{L-3/8\sigma_{ff}}\rho(z)dz \quad (15)$$

where ρ_a is the adsorbed phase density and L is the nanopore diameter. For nanopores with larger pore sizes, the gas in a nanopore is divided into an adsorbed phase and a free phase according to the gas density distribution in the nanopore,[43] and the adsorbed phase density is calculated separately.

2.4.2.2. Adsorbed Phase Density Calculation with the Ono−Kondo Lattice Model. The OK model is established based on lattice theory, which can characterize the adsorption of multilayer adsorption and supercritical gas. This model can calculate the corresponding adsorbed phase density by assuming the number of adsorbed layers. In this study, the OK model modified by Aranovich and Donohue[44] was adopted, which can accurately describe the gas interactions in multilayer adsorption. The correction process is described in detail in the literature.[44] The corrected thermodynamic equilibrium equation is
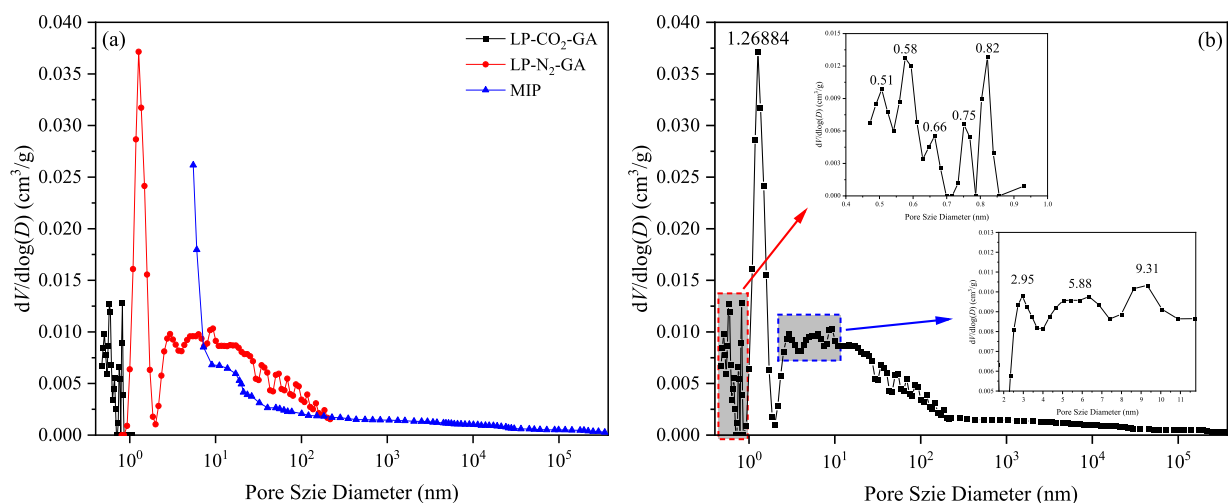
Figure 2. PSDs of the shale sample using the LP-CO$_2$-GA, LP-N$_2$-GA, and MIP methods. (a) Original result and (b) refactoring result.

$$\ln\left[\frac{x_i(1-x_b)}{x_b(1-x_i)}\right] + (z_1 x_{i+1} + z_2 x_i + z_1 x_{i-1} - z_0 x_b)\frac{\varepsilon}{k_B T}$$

$$+ \left(x_{i+1}^2 + x_{i-1}^2 - 2x_b^2 - \frac{2}{3}x_{i+1}^3 - \frac{2}{3}x_{i-1}^3 + \frac{4}{3}x_b^3\right)\frac{a_p}{k_B T}$$

$$+ \left(x_i^2 - x_b^2 - \frac{2}{3}x_i^3 + \frac{2}{3}x_b^3\right)\frac{a_m}{k_B T} = 0, \qquad i \geq 2 \tag{16}$$

$$\ln\left[\frac{x_1(1-x_b)}{x_b(1-x_1)}\right] + (z_1 x_2 + z_2 x_1 - z_0 x_b)\frac{\varepsilon}{k_B T}$$

$$+ \left(x_2^2 - 2x_b^2 - \frac{2}{3}x_2^3 + \frac{4}{3}x_b^3\right)\frac{a_p}{k_B T}$$

$$+ \left(x_1^2 - x_b^2 - \frac{2}{3}x_1^3 + \frac{2}{3}x_b^3\right)\frac{a_m}{k_B T} + \frac{\varepsilon_s}{k_B T} = 0,$$

$$i = 1 \tag{17}$$

where

$$x_i = \frac{\rho_{a,i}}{\rho_{am}} \tag{18}$$

$$x_b = \frac{\rho_b}{\rho_{am}} \tag{19}$$

where $\rho_{a,i}$ and ρ_b are the adsorbed phase density in layer i and the bulk phase density, ρ_{am} is the maximum adsorbed phase density, z_0 and z_2 are the bulk coordination number and the coordination number within any layer, and $z_1 = (z_0 - z_2)/2$. For the cubic lattice configuration, $z_0 = 6$, $z_1 = 1$, and $z_2 = 4$, ε and ε_s are the fluid–fluid energy parameter and fluid–solid energy parameter, and $\varepsilon = 0.432\varepsilon_{ff}$.[45] a_p and a_m are the interaction coefficients of neighboring molecules in the adjacent layer and the same layer, respectively, and k_B is the Boltzmann constant. The excess adsorption in the OK model can be given as

$$n_{ex} = 2C\sum_{i=1}^{n}(x_i - x_b) \tag{20}$$

where n is the number of adsorbed layers, and C is the total number of surface adsorption sites. The adsorbed phase density in the OK model can be expressed as

$$\rho_a = \frac{\sum_{i=1}^{n}\rho_{a,i}}{n} \tag{21}$$

3. RESULTS AND DISCUSSION

3.1. Pore Structure Characteristics of the Shale Sample. The pore structure characteristics of the shale sample obtained by the LP-CO$_2$-GA, LP-N$_2$-GA, and MIP methods are shown in Figure 2a. As shown in Figure 2a, the maximum peak value of the PSD appears at approximately 1.27 nm, which is more than three times higher than the other peaks, indicating that 1.27 nm micropores are distributed in large quantities in the shale sample, while other size micropores and mesopores are evenly distributed. Due to the overlapping pore size ranges characterized by the three methods, TPV and SSA were repeatedly calculated. Therefore, the effective pore size ranges of the three methods were selected to reconstruct the PSD. There are no pores measured in the overlapping range of LP-CO$_2$-GA and LP-N$_2$-GA, which can be directly connected; there is a wide range of overlap between LP-N$_2$-GA and MIP. The pore structure of the sample may be damaged, resulting in inaccurate test results as the injection pressure of the mercury increases during MIP. The overlapping part shall be subject to the results of LP-N$_2$-GA. Figure 2b and Table 2 show the

Table 2. TPV and SSA of the Shale Sample after the Combination of the Three Methods

pore size range (nm)	TPV ($\times 10^{-3}$ cm^3/g)	TPV percentage (%)	SSA (m^2/g)	SSA percentage (%)
micropore (0–2)	7.37	28.63	28.24	80.69
mesopore (2–50)	13.39	52.02	6.62	18.91
macropore (>50)	4.98	19.35	0.14	0.4
sample pore volume (cm^3/g)	25.74	sample SSA (m^2/g)	35.00	

reconstructed PSD result. The reconstructed sample pore volume is 25.74 cm^3/g, which is close to the sample pore volume of 24.58 cm^3/g in Section 2.1, indicating that the reconstructed PSD results are reliable. The TPV of the shale sample is characterized by a high proportion of mesopores (52.02%) and moderate proportions of micropores (28.63%) and macropores (19.35%). The reconstructed SSA of the shale
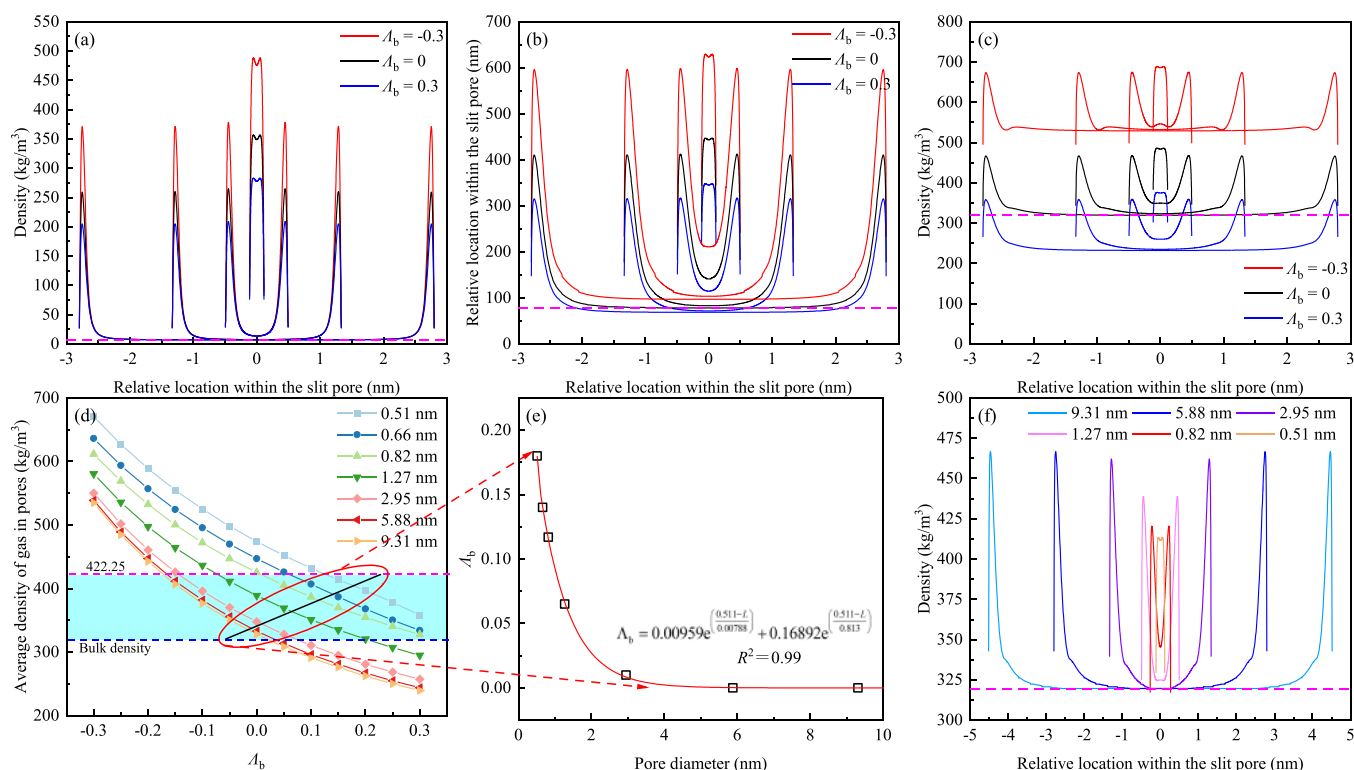
Figure 3. Relationship between Λ_b and CH_4 density distribution in pores in the SLD model. (a−c) CH_4 density distribution in pores with varying pore sizes under different pressures at 308.15 K; (d) the relationship between Λ_b and the average density of CH_4 in pores under 100 MPa at 308.15 K; (e) Λ_b values for different pore sizes in this study; and (f) CH_4 density distribution in the pores with varying pore sizes under 100 MPa at 308.15 K (Λ_b values were taken from Figure 3e).

sample is 35.00 m^2/g, characterized by a high proportion of micropores (80.69%) and low proportions of mesopores (18.91%) and macropores (0.4%). This indicates that the TPV of the shale sample is mainly associated with mesopores, while the SSA is mainly associated with micropores. Since the adsorption of shale mainly depends on the micropores and small mesopores in organic matter and clay minerals, pores of larger sizes contribute little to the adsorption. Therefore, in the following analysis, only the gas density distribution in pores with sizes ranging from 0 to 10 nm (0.51, 0.58, 0.66, 0.75, 0.82, 1.27, 2.95, 5.88, and 9.31 nm, Figure 2b) is considered.

3.2. Gas Density Distribution in Different Pore Sizes. The dominating pore sizes (0.51, 1.27, 2.95, and 5.88 nm) were selected from Section 3.1, and the CH_4 density distributions in pores with different sizes were studied using the SLD model. According to Pang et al.,[26] the covolume correction factor (Λ_b) in the SLD model represents the increase or decrease in the repulsive force in the adsorbed phase relative to the repulsive force in the bulk phase. In other words, the value of Λ_b can affect the calculation results of the SLD model for the density distribution of CH_4 in the pores. Therefore, in this study, the Λ_b values were set to −0.3, 0, and 0.3, respectively, and the gas density distribution under different pressures and pore sizes were calculated, and the results are shown in Figure 3a−c. Under low-pressure conditions, Λ_b affects the density of the adsorbed gas near the pore wall, with the density of the adsorbed gas decreasing as the Λ_b value increases. The density of CH_4 in the pore with a diameter of 0.51 nm is greater than that of the bulk phase, indicating clear pore-filling adsorption behavior. However, it is noteworthy that when Λ_b is −0.3, the density of CH_4 in the pore with a diameter of 0.51 nm is higher than the

critical density of the adsorbed phase, which is 422.25 kg/m^3, and this is unreasonable, especially under low-pressure conditions. As the pore size increases, the CH_4 peak density shifts toward the pore walls, and the density in the middle of the pore remains consistent with the bulk phase density. This indicates a transition from pore-filling adsorption to multilayer adsorption. At 10 MPa, increasing pressure affects the gas density distribution throughout the pore, with the Λ_b value being a significant factor. When Λ_b is −0.3, the gas density in the middle of pores with diameters of 2.95 and 5.88 nm is higher than the bulk phase density, whereas the opposite occurs when Λ_b is 0.3. At 100 MPa, these phenomena occur in all pore sizes and become more prominent. However, the density distribution of CH_4 in pores with diameters of 2.95 and 5.88 nm is reasonable at $\Lambda_b = 0$.

To obtain reasonable values of Λ_b in pores of different sizes, this study used the SLD model to calculate the average density of CH_4 in different-sized pores under ultra-high pressure (100 MPa), with Λ_b ranging from −0.3 to 0.3, as shown in Figure 3d. The blue region in Figure 3d (between the lower limit of bulk density and the upper limit of 422.25 kg/m^3) represents the effective range of CH_4 average density in the pores. When Λ_b is negative, the average density of CH_4 in the pores is found to be higher than the critical density (422.25 kg/m^3) of the CH_4 adsorption phase. When Λ_b is positive, the average density of gas in pores larger than 1 nm is lower than the bulk density. Therefore, fixing a value for Λ_b cannot accurately characterize the gas density distribution in pores of different sizes, and the value of Λ_b needs to be chosen according to the pore size. This study assumes that the adsorption mechanism in shale is the combination of micropore filling and mesopore multilayer
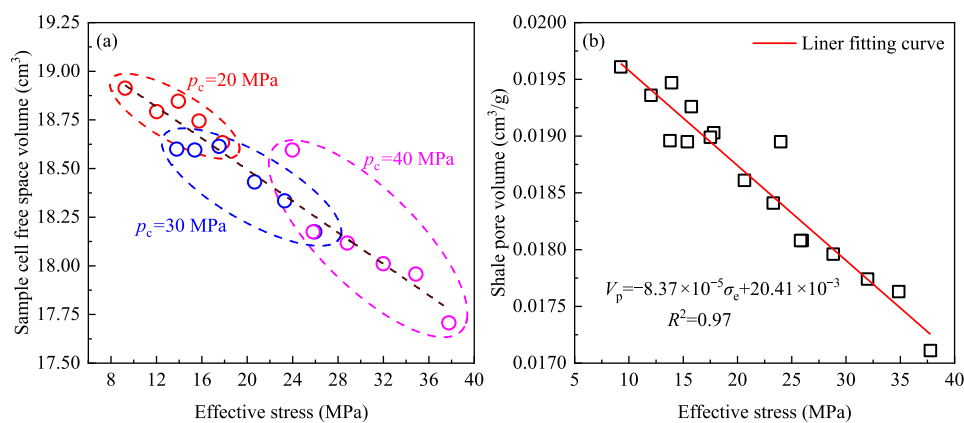
Figure 4. Variation in the free volume of the sample cell and pore volume of the shale sample under effective stress. (a) Free volume of the sample cell and (b) shale sample pore volume.

adsorption, and that only small enough micropores can reach the adsorption phase density of 422.25 kg/m^3 under ultra-high pressure. Based on these assumptions, it can be inferred that as the pore size increases, Λ_b gradually decreases and approaches 0, as shown in Figure 3e, and the mathematical relationship between Λ_b and L is shown in eq 22. The density distribution of CH$_4$ in pores of different sizes calculated using the chosen Λ_b values under ultra-high pressure (100 MPa) is consistent with the assumed adsorption mechanism, as shown in Figure 3f.

$$\Lambda_b = 0.00959\, e^{(0.511-L/0.00788)} + 0.16892\, e^{(0.511-L/0.813)} \tag{22}$$

**3.3. Experimental Results of Methane Adsorption of Massive Shale.** *3.3.1. Effect of Effective Stress on the Pore Volume of the Shale Sample.* The dead volumes of the sample cell measured by the helium expansion method are between 9.25 and 9.76 cm^3, and the dead volume of the sample cell is taken as their average value (9.45 cm^3) in this study. Figure 4a shows the free volume of the sample cell under effective stress after placing the massive shale sample in the sample cell. The relationship between the free volume of the sample cell and the effective stress was obtained by changing the confining pressure and pore pressure. The free volume of the sample cell decreases linearly with increasing effective stress. In this experimental device, the difference between the free volume and the dead volume is the effective pore volume of the shale sample. The unit pore volume of the shale sample in the absence of stress was 20.41 × 10^{-3} cm^3/g. The pore volume of massive shale is lesser compared to that discussed in Sections 2.1 and 3.1, indicating the presence of some non-interconnected isolated pores in the massive shale. This implies that the SSA of massive shale is smaller than that of granular shale, resulting in a reduced number of corresponding adsorption sites as compared to the granular samples. This would lead to an overestimation of the adsorption capacity of the shale. Figure 4b shows the relationship between the effective pore volume of the sample and effective stress. The effective pore volume decreases linearly with increasing effective stress, and Pang et al.[46] also found similar results. According to eq 23,[47] the pore volume compressibility of this shale sample can be calculated

$$C_{pv} = \frac{1}{V_p}\left(\frac{\partial V_p}{\partial \sigma_e}\right) \tag{23}$$

where C_{pv} is the pore volume compressibility, V_p is the sample pore volume, and σ_e is the effective stress, which is the difference between volumetric stress and pore pressure; C_{pv} of the shale sample in this study is -8.37×10^{-5} MPa^{-1}, which is close to the pore volume compressibility of shale samples presented in the work of Santos and Akkutlu.[37]

3.3.2. CH$_4$ Adsorption Isotherms of the Massive Shale. Figure 5 compares the CH$_4$ adsorption isotherms of massive and
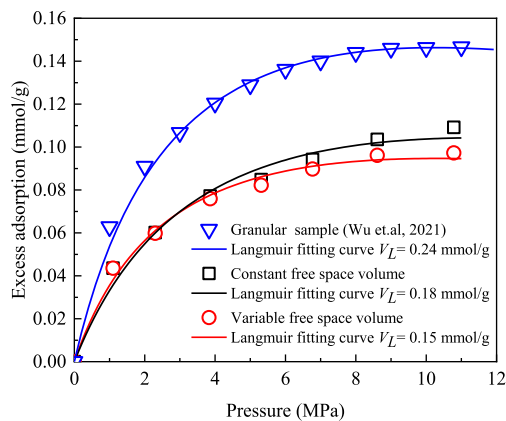
Figure 5. Influence of free volume on CH$_4$ adsorption isotherm in massive shale.

granular shale samples fitted using the Langmuir model, where the CH$_4$ isotherm of the granular shale sample was obtained from previous work under the same experimental conditions. The Langmuir volume (V_L) results indicate that the V_L of the granular sample is 1.6 times that of the massive sample, suggesting that the granular sample has a higher adsorption capacity than the massive sample. However, the massive sample is a better representation of the actual situation in shale reservoirs, and the results of the granular sample may overestimate the gas content in shale. Additionally, neglecting the changes in the pore volume of massive shale under effective stress can overestimate the shale adsorption capacity, indicating that pore volume should be considered in massive shale adsorption experiments.

3.4. Adsorption Curve Fitting Considering the Participation of Nanopores of Multiple Sizes. The massive shale sample has an intact pore structure, and the connected pores in the sample participate in the adsorption. Based on the

assumption of the adsorption mechanism in Section 3.2, pores with varying pore sizes contribute differently to the total adsorption amount. According to the PSD, the adsorption amount measured by the adsorption experiment can be expressed as

$$n_{\text{ex}} = \sum n_{\text{ex,PSD}} \tag{24}$$

where $n_{\text{ex,PSD}}$ is the excess adsorption amount of dominant pores selected based on the PSD. The SLD model is used to characterize the adsorption behavior of pores with varying pore sizes, and the excess adsorption amount based on the SLD model is expressed as

$$n_{\text{ex}} = \sum_{i=1}^{n} \frac{A_i}{2} \int_{3/8\sigma_{\text{ff}}}^{L_i - 3/8\sigma_{\text{ff}}} (\rho_{L_i}(z) - \rho_{\text{b}}) \mathrm{d}z \tag{25}$$

where n represents the number of dominant pore sizes, A is the total SSA of the pores, and V is the TPV of the pores. The deformation of the slit-type pore structure under effective stress based on the SLD model, as shown in Figure 6, assumes that the
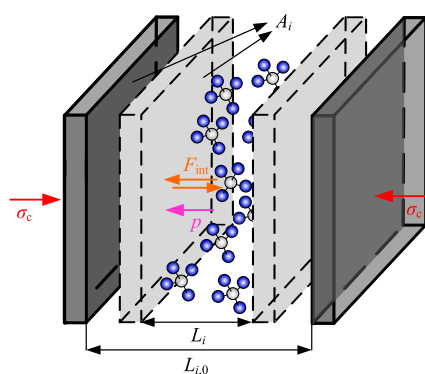
Figure 6. Schematic of the deformation of the slit-type pore structure under effective stress.

change in the pore volume only changes the pore size while the SSA of the pore remains unchanged. This is expressed in eqs 26 and 27 as follows

$$A_i = C_{V_{i,0}} A_{i,0} \tag{26}$$

$$L_i = L_{i,0}(1 + C_{\text{L}}\sigma_{\text{e}}) \tag{27}$$

where C_{V} is the connected porosity, C_{L} represents the coefficient of the change in pore size caused by pressure and adsorption, and the subscript $i,0$ is the initial value of the pore structure of the i-th pore size. Assuming that the pore connectivity in shale is uniform, the dominant pore sizes and the corresponding pore volume were selected by PSD to fit the adsorption curve of massive shale, and finally, the pore connectivity and the pore size variation coefficient during the adsorption process were obtained. The dominant pore sizes involved in adsorption and the corresponding pore volumes and SSAs are shown in Table 3.

Figure 7a shows the fitting results obtained by using eq 25 to fit the excess adsorption isotherm of massive shale, reflecting when pores with different sizes participate in adsorption. The pore connectivity and pore size change coefficient are 0.70% and -2.96×10^{-4} MPa^{-1}, respectively. It was found that the pore size change coefficient was consistent with the pore volume compression coefficient in Section 3.3. On the one hand, it was assumed that the SSA remains unchanged during the adsorption process and that the change in the pore volume is only reflected

Table 3. Dominant Pore Size Involved in Adsorption and the Corresponding Pore Volume and Specific Surface Area in This Study[a]

| i	$L_{i,0}$ (nm)	$V_{i,0}$ ($\times 10^{-3}$ cm^3/g)	$A_{i,0}$ (m^2/g)
1	0.51	0.64	5.02
2	0.58	0.59	4.07
3	0.67	0.16	0.96
4	0.75	0.13	0.69
5	0.82	0.24	1.17
6	1.27	5.61	17.67
7	2.95	2.34	3.17
8	5.88	2.48	1.69
9	9.31	1.57	0.67

[a]Note: $A_{i,0}$ is calculated by $4V_{i,0}/L_{i,0}$.

in change in the pore size. On the other hand, the pore deformation caused by adsorption is very small under effective stress.[48,49] The pore SSA dominated the adsorption amount, and pores with a size of 1.27 nm contributed to approximately half of the adsorption amount. According to the pore size, the adsorption curve was divided into two trends. For micropores, under a low pressure, the smaller the pore size, the faster the increase in the excess adsorption amount. With increasing pressure, the change in the excess adsorption amount gradually tends to be stable and shows a downward trend. For mesopores, due to the large pore size, the adsorption potentials of two walls do not affect each other, and the adsorption behavior is mostly multilayer adsorption. The excess adsorption amount increases gradually with increasing pressure. When the pressure reaches a certain value, the excess adsorption amount will reach a peak value, and then there will be a downward trend,[17,34] but this trend will have a significant lag compared with that of micropores. Figure 7b shows the contribution of pores with varying pore sizes to the total excess adsorption amount. It can be found that the contribution of micropores to the adsorption amount plays a dominant role under low-pressure conditions. However, the contribution of mesopores to the adsorption amount gradually increases with increasing pressure, and the threshold micropores and mesopores are of a pore size of approximately 1 nm.
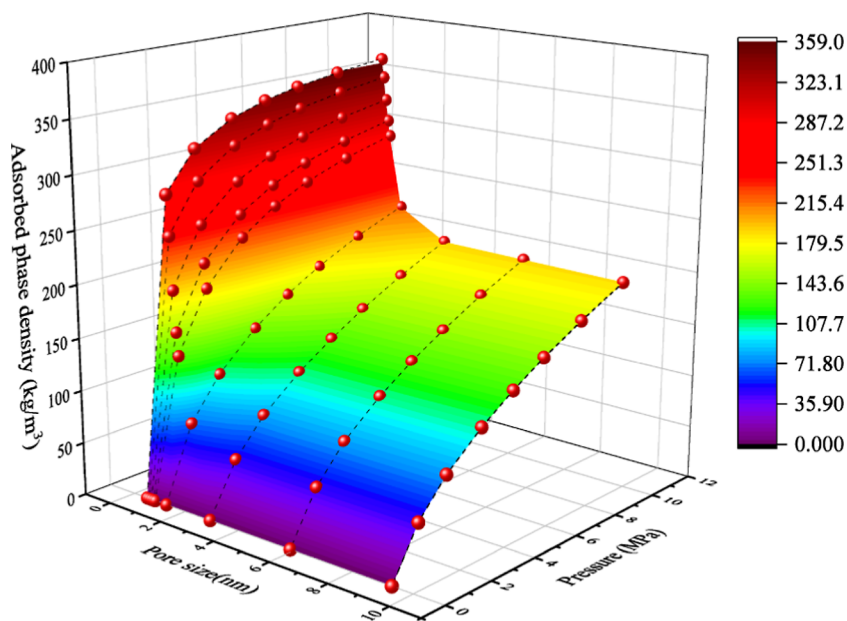
3.5. Calculation of Adsorbed Phase Density with Different Pore Sizes. Assuming the mechanisms of micropore filling and multilayer adsorption in mesopores, the adsorption phase density of micropores can be expressed by calculating the average gas density within the micropores using the SLD model (eq 15). At present, the mainstream method for the division of the adsorbed phase in mesopores is to artificially divide the gas density distribution into the adsorbed phase and free phase. However, for the adsorption phase density of mesopores, although the SLD model can calculate the gas density distribution within the pores in the form of multilayer adsorption, previous work has shown that the gas density distribution calculated by the SLD model has a transition region, making it difficult to accurately distinguish between the adsorbed and free phases. This may result in erroneous judgments regarding the width of the adsorption phase and can lead to errors in calculating the adsorption phase density and further result in incorrect determination of absolute adsorption amounts. This study employed the OK model, which assumes a certain number of adsorption layers, combined with the SLD model to calculate the gas density distribution in mesopores and determine the adsorption phase density. Based on the CH$_4$
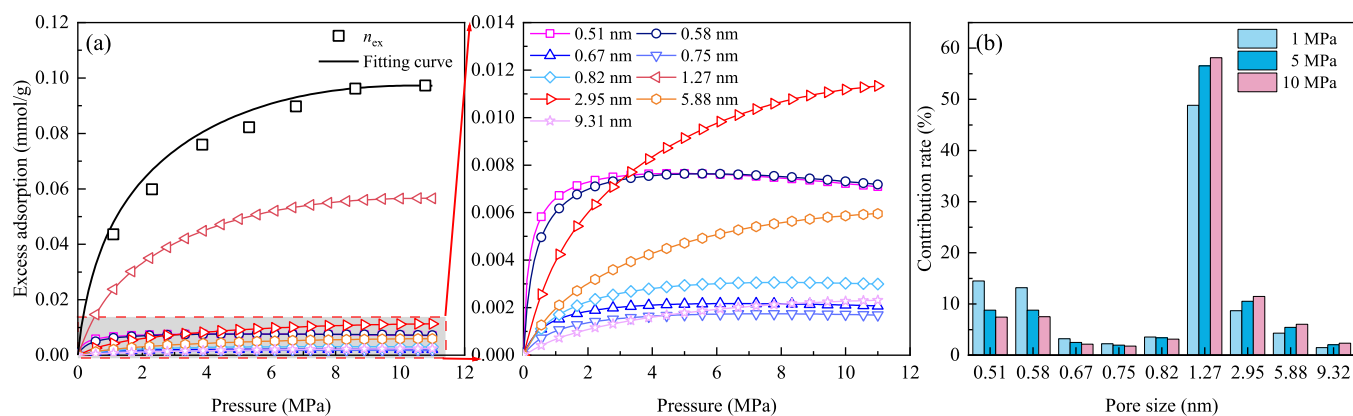
Figure 7. Excess adsorption isotherms with the participation of nanopores with varying pore sizes. (a) Fitting results of the method in this study and (b) contribution of the adsorption amount of pores with varying pore sizes to the total adsorption amount with increasing pressure.
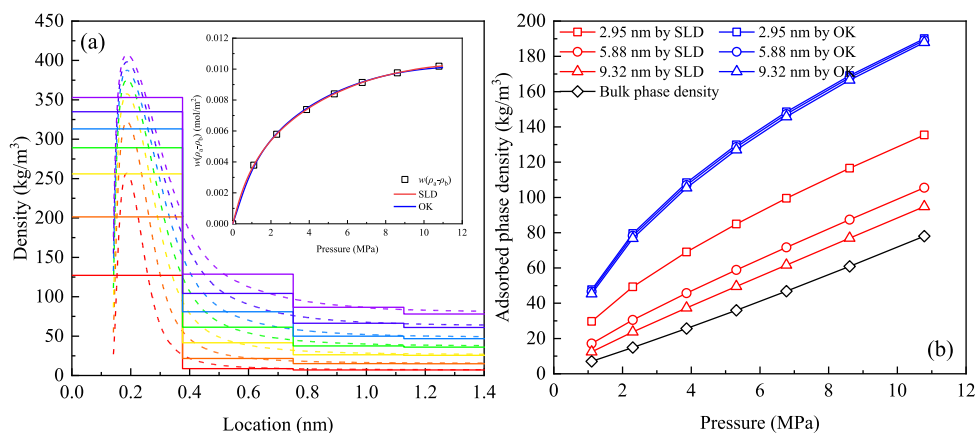
Figure 8. Gas density distribution in mesoporous pores calculated by the SLD model and OK model. (a) Comparison of the gas density distributions calculated by the SLD model and the density of each adsorption layer calculated by the OK model. (b) Adsorbed phase densities in mesopores calculated by the SLD model and OK model.

Figure 9. Adsorbed phase densities in nanopores with varying pore sizes.

density distribution in mesopores calculated by the SLD model and the diameter of the CH_4 molecules, assuming a three-layer adsorption, and considering the interactions between gas

molecules, the gas quantity in the mesopores was fitted using the OK model introduced in Section 2.4.2.2, as shown in Figure 8a. The fitting parameters in the OK model were as follows: $\varepsilon_s/$

$kT = -3.68$, $a_p/kT = -1.52$, $a_m/kT = 0.97$, and $\rho_a = 422.25$ kg/m³.

From Figure 8a, it is apparent that the fitting results obtained from the OK model are in good agreement with the excess adsorption calculated by the SLD model. Furthermore, the density of each adsorption layer, as calculated by the OK model, corresponds well with the gas density distribution in the mesopores computed by the SLD model. This suggests that the joint use of the SLD model and the OK model is a viable approach for determining the density of the adsorption phase in mesopores. Figure 8b illustrates the adsorption phase density in mesopores obtained by applying the aforementioned method and eqs 15 and 20. Specifically, the adsorbed phase density calculated using the OK model is higher than that obtained from the SLD model. Moreover, the adsorption phase density obtained from the OK model is consistent across different pore sizes, indicating that it is independent of pore size, while the adsorption phase density obtained from the SLD model decreases as the pore size increases. For mesopores, it is possible that the superposition of adsorption between two pore walls is not accurate. Assuming single-wall adsorption, the adsorption phase density calculated using the OK model is more consistent with the proposed adsorption mechanism for mesopores in this study. Therefore, in this study, the adsorption phase density in micropores was determined using the SLD model, while the adsorption phase density in mesopores was calculated by combining the SLD model and the OK model, and eqs 15 and 20 were utilized to determine the adsorption phase density in micropores and mesopores, respectively.

Figure 9 shows the density of the adsorbed phase in pores of different sizes. The density of the adsorbed phase in micropores smaller than 1 nm is significantly higher than that in mesopores, and the difference between them gradually decreases with increasing pressure. When the pressure is 10 MPa, the adsorbed phase density in micropores is approximately twice that of mesopores. The adsorbed phase density in the pores with sizes of 1−2 nm has an obvious transition trend, and the adsorption mechanism in these pores gradually changes from pore filling to multilayer adsorption.

3.6. Calculation of Absolute Adsorption Amount of Massive Shale. The selection of the adsorbed phase density value is of great significance in the estimation of the adsorption amount. Santos and Akkutlu[37] found that the use of different adsorbed phase densities would lead to great differences in the calculated absolute adsorption amount. Using the adsorbed phase density calculation method proposed in this study, the absolute adsorption amount of massive shale was calculated by eq 28 and compared with the absolute adsorption amount calculated by the commonly used Langmuir, SDR, and SLD models, as shown in Figure 10.

$$n_{ab} = n_{ex} \frac{\rho_a}{\rho_a - \rho_b} \tag{28}$$

In Figure 10, the Langmuir and SDR models used fixed adsorbed phase densities (421 and 373 kg/m³)[50] to convert the absolute adsorption amount according to eq 28. Similar adsorbed phase densities lead to similar absolute adsorption amounts, but it can also be found that the smaller the adsorbed phase density, the greater the absolute adsorption amount. Equation 28 is used to calculate the average adsorbed phase density obtained by the method proposed in this study, which was found to be approximately 217 kg/m³, which is far less than
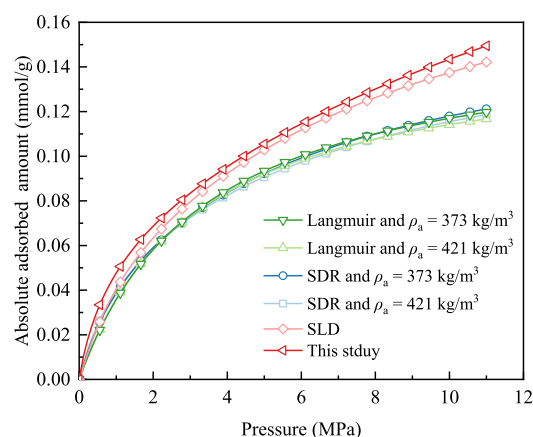

Figure 10. Absolute adsorption amount of massive shale calculated by multiple methods.

the commonly used CH₄ adsorbed phase densities. The adsorbed phase density of mesopores is considered in the adsorbed phase calculation method proposed in this study. The adsorption mechanism of mesopores is multilayer adsorption, and the adsorbed phase density decreases as the adsorbed phase volume increases.[51] However, the average adsorbed phase density (217 kg/m³) obtained in this study also has no reference value for engineering practice, since the unreasonable phenomenon that the bulk density of CH₄ is higher than this value will arise when the pressure increases. Therefore, there is a limit to the conversion of the absolute adsorption capacity through a fixed adsorbed phase density. The method presented in this study and the SLD model were used to convert the absolute adsorption amount by varying the adsorbed phase density. The pore size selected by the SLD model is the dominant pore size of 1.27 nm in the sample, and the adsorption mechanism is equivalent to micropore filling. Due to the major contribution of 1.27 nm pores to adsorption, the absolute adsorption amount converted by the SLD model is closest to that of the method presented in this study. In summary, the shale adsorption mechanism is mainly composed of micropore filling, but mesoporous multilayer adsorption cannot be ignored. In addition, the adsorbed phase density should be a function of temperature, pressure, and pore size. It is necessary to calculate the adsorbed phase density according to the adsorption mechanism of pores with varying pore sizes and then convert the absolute adsorption amount.

3.7. Shale GIP Estimation. The shale GIP consists of adsorbed gas and free gas. In this study, the adsorbed gas content and free gas content of the massive shale sample were calculated using eqs 29 and 30, respectively.

$$G_a = \begin{cases} \sum_i^n \frac{C_v A_i}{2} \int_{3/8\sigma_{ff}}^{L_i - 3/8\sigma_{ff}} \rho_{L_i}(z)dz & L_i \leq 2 \text{ nm} \\ \sum_i^n C_v A_i \sum_{i=1}^3 x_i & L_i > 2 \text{ nm} \end{cases} \tag{29}$$

$$G_f = C_{STP} \cdot \rho_b \cdot \left(V_p (1 - C_{pv} \cdot D(g_s - g_p)) - C_v \sum_{i=1}^n V_{a,i} \right) \tag{30}$$
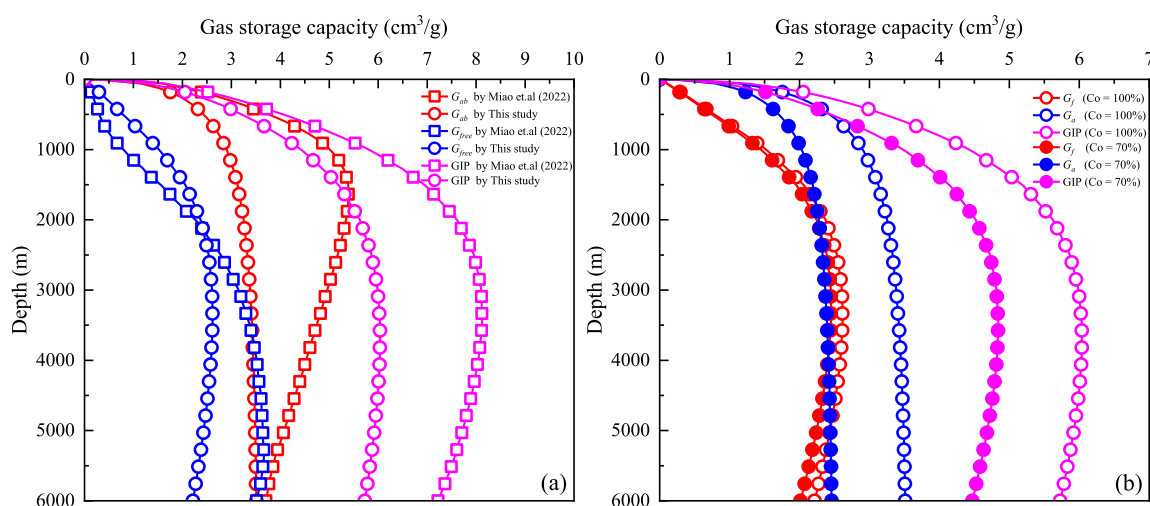
Figure 11. GIP estimation of massive shale. (a) Considering PSD and pore volume compressibility. (b) Considering connected porosity.

$$V_{a,i} = \begin{cases} \dfrac{1}{4} A_i L_i (1 + C_L \cdot D(g_s - g_p)) & L_i \leq 2 \text{ nm} \\ 3\sigma_{ff} A_i & L_i > 2 \text{ nm} \end{cases} \quad (31)$$

where G_a and G_f represent the content of the adsorbed gas and free gas, respectively, C_{STP} is the coefficient of unit conversion from mass to volume for CH_4 and equal to 1.4×10^3 cm³/g, D represents the buried depth, g_s and g_p represent the stress gradient and pressure gradient, respectively, and V_a represents the volume of the adsorbed phase. The geological parameters are consistent with the literature.[32]

Figure 11a shows the GIP of the massive shale sample in this study considering the PSD and pore volume compressibility and compares it with the GIP estimated in a previous study,[32] where the calculation was based on the average pore size (3.89 nm) by utilizing the SLD model. It was observed that the free gas content estimated using the average pore size was relatively low compared to the adsorbed gas content, especially before the burial depth of 2000 m. This can be attributed to the wrong distinction between the adsorbed and free phase ranges in the mesopores by the SLD model at low pressure, resulting in an overestimation of the adsorbed gas and an underestimation of the free gas content. For free gas, due to the compressibility of pore volume, with the increase of burial depth, the in situ stress is dominant in the effective stress relative to pore pressure, resulting in the storage space of free gas gradually decreasing with the increase of burial depth, and then leading to the reduction of free gas content. In comparison to the average pore size calculation method, the analysis of the PSD reveals that the content of adsorbed gas does not exhibit a decreasing trend with the increasing burial depth. This phenomenon can be attributed to the fact that the contribution of micropores, which constitute a substantial proportion of the PSD, to the adsorption process has been taken into consideration. Under high-pressure conditions, the density of the adsorbed phase in the micropores is relatively unaffected by temperature, which explains the absence of a declining trend in the content of adsorbed gas with increasing burial depth. Figure 11b depicts the GIP while taking connected porosity into account. Based on the adsorption experiment of massive shale under constrained conditions, it has been observed that the actual porosity of massive shale is smaller than that measured by granular samples. This is due to the existence of dead pores in the complete massive shale that do not

participate in adsorption. Consequently, the gas contained in such dead pores will not be extractable during mining. To obtain an accurate estimation of GIP, it is, therefore, imperative to consider the actual PSD in shale samples and to calculate the adsorbed gas content based on the corresponding adsorption mechanism. Moreover, the connected porosity of shale as well as the compressibility of pore volume must also be taken into consideration.

4. CONCLUSIONS

In this study, a CH_4 adsorption experiment of massive shale under effective stress was carried out, and the occurrence mechanism of shale gas was preliminarily explored at the core scale. The main conclusions are as follows:

(1) The massive shale samples possess non-connected pores, resulting in significantly lower adsorption capacity compared to granular samples. The pore volume of massive shale linearly decreases with increasing effective stress, and ignoring the change in pore volume during adsorption experiments leads to an overestimation of shale adsorption capacity by approximately 20%. Micropores play a dominant role in adsorption at low pressures. With increasing pressure, the adsorption capacity of micropores tends to saturate, while the contribution of mesopores to adsorption gradually increases.

(2) The covolume parameter Λ_b in the SLD model plays a crucial role in accurately characterizing the gas density distribution within pores, and incorporating a functional relationship between Λ_b and pore size can render the gas density distribution calculated by the SLD model more realistic. While micropore filling dominates shale adsorption, multilayer surface adsorption of mesopores cannot be neglected. The combination of the SLD model and the OK model can be utilized to effectively characterize the density of adsorption layers in mesopores and accurately determine the density of the adsorbed phase. It is worth noting that the CH_4 adsorbed phase density in micropores is approximately twice that of mesopores.

(3) In order to accurately estimate the shale gas reserves, it is necessary to take into account the actual PSD in shale samples and calculate the adsorbed gas content based on the corresponding adsorption mechanism. Additionally, it

is important to consider the connected porosity and pore volume compressibility in shale.

AUTHOR INFORMATION

Corresponding Author

Di Wu − *School of Mechanics and Engineering, Liaoning Technical University, Fuxin 123000, China; Liaoning Key Laboratory of Mining Environment and Disaster Mechanics, Liaoning Technical University, Fuxin 123000, China;* orcid.org/0000-0002-9662-0022; Email: wudi202@126.com

Authors

Feng Miao − *School of Mechanics and Engineering, Liaoning Technical University, Fuxin 123000, China*

Nan Jia − *China Coal Technology and Engineering Group Corp Shenyang Research Institute, Fushun 113122, China; State Key Laboratory of Coal Mine Safety Technology, Fushun 113122, China*

Xiaochun Xiao − *School of Mechanics and Engineering, Liaoning Technical University, Fuxin 123000, China; Liaoning Key Laboratory of Mining Environment and Disaster Mechanics, Liaoning Technical University, Fuxin 123000, China*

Weiji Sun − *School of Mechanics and Engineering, Liaoning Technical University, Fuxin 123000, China*

Xin Ding − *School of Mechanics and Engineering, Liaoning Technical University, Fuxin 123000, China; Liaoning Key Laboratory of Mining Environment and Disaster Mechanics, Liaoning Technical University, Fuxin 123000, China;* orcid.org/0000-0002-9136-6299

Wenbo Zhai − *School of Mechanics and Engineering, Liaoning Technical University, Fuxin 123000, China*

Xintong Chen − *School of Mechanics and Engineering, Liaoning Technical University, Fuxin 123000, China*

Complete contact information is available at:
https://pubs.acs.org/10.1021/acsomega.3c00836

Notes

The authors declare no competing financial interest.

REFERENCES

(1) Klewiah, I.; Berawala, D. S.; Alexander Walker, H. C.; Andersen, P. Ø.; Nadeau, P. H. Review of Experimental Sorption Studies of CO2 and CH4 in Shales. *J. Nat. Gas Sci. Eng.* 2020, 73, 103045.

(2) Vidic, R. D.; Brantley, S. L.; Vandenbossche, J. M.; Yoxtheimer, D.; Abad, J. D. Impact of Shale Gas Development on Regional Water Quality. *Science* 2013, 340, 1235009.

(3) Zou, C.; Dong, D.; Wang, Y.; Li, X.; Huang, J.; Wang, S.; Guan, Q.; Zhang, C.; Wang, H.; Liu, H.; Bai, W.; Liang, F.; Lin, W.; Zhao, Q.; Liu, D.; Yang, Z.; Liang, P.; Sun, S.; Qiu, Z. Shale Gas in China: Characteristics, Challenges and Prospects (II). *Pet. Explor. Dev.* 2016, 43, 182−196.

(4) Ma, X.; Xie, J. The Progress and Prospects of Shale Gas Exploration and Development in Southern Sichuan Basin, SW China. *Pet. Explor. Dev.* 2018, 45, 172−182.

(5) Lenhard, L. G.; Andersen, S. M.; Coimbra-Araújo, C. H. Energy-Environmental Implications Of Shale Gas Exploration In Paraná Hydrological Basin, Brazil. *Renewable Sustainable Energy Rev.* 2018, 90, 56−69.

(6) Zhou, S.; Wang, H.; Li, B.; Li, S.; Sepehrnoori, K.; Cai, J. Predicting Adsorbed Gas Capacity of Deep Shales under High Temperature and Pressure: Experiments and Modeling. *Adv. Geo-Energy Res.* 2022, 6, 482−491.

(7) Yan, W.; Zou, L.; Li, H.; Deng, J.; Ge, H.; Wang, H. Investigation of Casing Deformation during Hydraulic Fracturing in High Geo-Stress Shale Gas Play. *J. Pet. Sci. Eng.* 2017, 150, 22−29.

(8) Dang, W.; Zhang, J.; Nie, H.; Wang, F.; Tang, X.; Wu, N.; Chen, Q.; Wei, X.; Wang, R. Isotherms, Thermodynamics and Kinetics of Methane-Shale Adsorption Pair under Supercritical Condition: Implications for Understanding the Nature of Shale Gas Adsorption Process. *Chem. Eng. J.* 2020, 383, 123191.

(9) Curtis, J. B. Fractured Shale-Gas Systems. *AAPG Bull.* 2002, 86, 1921.

(10) Brochard, L.; Vandamme, M.; Pellenq, R. J.-M.; Fen-Chong, T. Adsorption-Induced Deformation of Microporous Materials: Coal Swelling Induced by $CO_2 − CH_4$ Competitive Adsorption. *Langmuir* 2012, 28, 2659−2670.

(11) Rexer, T. F. T.; Benham, M. J.; Aplin, A. C.; Thomas, K. M. Methane Adsorption on Shale under Simulated Geological Temperature and Pressure Conditions. *Energy Fuels* 2013, 27, 3099−3109.

(12) Heller, R.; Zoback, M. Adsorption of Methane and Carbon Dioxide on Gas Shale and Pure Mineral Samples. *J. Unconv. Oil Gas Resour.* 2014, 8, 14−24.

(13) Gasparik, M.; Bertier, P.; Gensterblum, Y.; Ghanizadeh, A.; Krooss, B. M.; Littke, R. Geological Controls on the Methane Storage Capacity in Organic-Rich Shales. *Int. J. Coal Geol.* 2014, 123, 34−51.

(14) Pang, Y.; Soliman, M. Y.; Deng, H.; Xie, X. Experimental and Analytical Investigation of Adsorption Effects on Shale Gas Transport in Organic Nanopores. *Fuel* 2017, 199, 272−288.

(15) Pang, W.; He, Y.; Yan, C.; Jin, Z. Tackling the Challenges in the Estimation of Methane Absolute Adsorption in Kerogen Nanoporous Media from Molecular and Analytical Approaches. *Fuel* 2019, 242, 687−698.

(16) Bai, J.; Kang, Y.; Chen, M.; Chen, Z.; You, L.; Li, X.; Chen, G. Impact of Surface Chemistry and Pore Structure on Water Vapor Adsorption Behavior in Gas Shale. *Chem. Eng. J.* 2020, 402, 126238.

(17) Xiong, F.; Rother, G.; Tomasko, D.; Pang, W.; Moortgat, J. On the Pressure and Temperature Dependence of Adsorption Densities and Other Thermodynamic Properties in Gas Shales. *Chem. Eng. J.* 2020, 395, 124989.

(18) Langmuir, I. THE ADSORPTION OF GASES ON PLANE SURFACES OF GLASS, MICA AND PLATINUM. *J. Am. Chem. Soc.* 1918, 40, 1361−1403.

(19) Sakurovs, R.; Day, S.; Weir, S.; Duffy, G. Temperature Dependence of Sorption of Gases by Coals and Charcoals. *Int. J. Coal Geol.* 2008, 73, 250−258.

(20) Qi, R.; Ning, Z.; Wang, Q.; Huang, L.; Wu, X.; Cheng, Z.; Zhang, W. Measurements and Modeling of High-Pressure Adsorption of CH4 and CO2 on Shales. *Fuel* 2019, 242, 728−743.

(21) Sakurovs, R.; Day, S.; Weir, S.; Duffy, G. Application of a Modified Dubinin−Radushkevich Equation to Adsorption of Gases by Coals under Supercritical Conditions. *Energy Fuels* 2007, 21, 992−997.

(22) Chen, L.; Jiang, Z.; Liu, K.; Ji, W.; Wang, P.; Gao, F.; Hu, T. Application of Langmuir and Dubinin−Radushkevich Models to Estimate Methane Sorption Capacity on Two Shale Samples from the Upper Triassic Chang 7 Member in the Southeastern Ordos Basin, China. *Energy Explor. Exploit.* 2017, 35, 122−144.

(23) Zhou, S.; Ning, Y.; Wang, H.; Liu, H.; Xue, H. Investigation of Methane Adsorption Mechanism on Longmaxi Shale by Combining the Micropore Filling and Monolayer Coverage Theories. *Adv. Geo-Energy Res.* 2018, 2, 269−281.

(24) Pang, W.; Jin, Z. Ono-Kondo Lattice Model for Propane Multilayer Adsorption in Organic Nanopores in Relation to Shale Gas. *Fuel* 2019, 235, 158−166.

(25) Huang, H.; Li, R.; Jiang, Z.; Li, J.; Chen, L. Investigation of Variation in Shale Gas Adsorption Capacity with Burial Depth: Insights from the Adsorption Potential Theory. *J. Nat. Gas Sci. Eng.* **2020**, *73*, 103043.

(26) Pang, Y.; Hu, X.; Wang, S.; Chen, S.; Soliman, M. Y.; Deng, H. Characterization of Adsorption Isotherm and Density Profile in Cylindrical Nanopores: Modeling and Measurement. *Chem. Eng. J.* **2020**, *396*, 125212.

(27) Wu, D.; Miao, F.; Liu, X.; Xiao, X.; Zhai, W. Prediction of High-Pressure Adsorption of CH4 and CO2 in Shale. *Int. J. Greenh. Gas Control* **2021**, *110*, 103440.

(28) Wu, D.; Chen, X.; Miao, F.; Xiao, X.; Zhai, W. Absolute Adsorption Calculation of Shale Gas Based on the Ono−Kondo Lattice Model. *Energy Fuels* **2023**, *37*, 328−338.

(29) Chen, G.; Lu, S.; Zhang, J.; Xue, Q.; Han, T.; Xue, H.; Tian, S.; Li, J.; Xu, C.; Pervukhina, M. Keys to Linking GCMC Simulations and Shale Gas Adsorption Experiments. *Fuel* **2017**, *199*, 14−21.

(30) Zhao, T.; Li, X.; Zhao, H.; Li, M. Molecular Simulation of Adsorption and Thermodynamic Properties on Type II Kerogen: Influence of Maturity and Moisture Content. *Fuel* **2017**, *190*, 198−207.

(31) Song, W.; Yao, J.; Ma, J.; Li, A.; Li, Y.; Sun, H.; Zhang, L. Grand Canonical Monte Carlo Simulations of Pore Structure Influence on Methane Adsorption in Micro-Porous Carbons with Applications to Coal and Shale Systems. *Fuel* **2018**, *215*, 196−203.

(32) Miao, F.; Wu, D.; Liu, X.; Xiao, X.; Zhai, W.; Geng, Y. Methane Adsorption on Shale under in Situ Conditions: Gas-in-Place Estimation Considering in Situ Stress. *Fuel* **2022**, *308*, 121991.

(33) Ambrose, R. J.; Hartman, R. C.; Diaz-Campos, M.; Akkutlu, I. Y.; Sondergeld, C. H. Shale Gas-in-Place Calculations Part I: New Pore-Scale Considerations. *SPE J.* **2012**, *17*, 219−229.

(34) Feng, G.; Zhu, Y.; Chen, S.; Wang, Y.; Ju, W.; Hu, Y.; You, Z.; Wang, G. G. X. Supercritical Methane Adsorption on Shale over Wide Pressure and Temperature Ranges: Implications for Gas-in-Place Estimation. *Energy Fuels* **2020**, *34*, 3121−3134.

(35) Ambrose, R. J.; Hartman, R. C.; Akkutlu, I. Y. Multi-Component Sorbed-Phase Considerations for Shale Gas-in-Place Calculations. *All Days*; SPE: Oklahoma City, Oklahoma, USA, 2011.

(36) Kang, S. M. . M.; Fathi, E. .; Ambrose, R. J. . J.; Akkutlu, I. Y. . Y.; Sigal, R. F. . F. Carbon Dioxide Storage Capacity of Organic-Rich Shales. *SPE J.* **2011**, *16*, 842−855.

(37) Santos, J. M. . M.; Akkutlu, I. Y. . Y. Laboratory Measurement of Sorption Isotherm Under Confining Stress With Pore-Volume Effects. *SPE J.* **2013**, *18*, 924−931.

(38) Etminan, S. R.; Javadpour, F.; Maini, B. B.; Chen, Z. Measurement of Gas Storage Processes in Shale and of the Molecular Diffusion Coefficient in Kerogen. *Int. J. Coal Geol.* **2014**, *123*, 10−19.

(39) Mohammad, S.; Fitzgerald, J.; Robinson, R. L.; Gasem, K. A. M. Experimental Uncertainties in Volumetric Methods for Measuring Equilibrium Adsorption. *Energy Fuels* **2009**, *23*, 2810−2820.

(40) Gasem, K. A. M.; Gao, W.; Pan, Z.; Robinson, R. L. A Modified Temperature Dependence for the Peng−Robinson Equation of State. *Fluid Phase Equilib.* **2001**, *181*, 113−125.

(41) Chen, J. H.; Wong, D. S. H.; Tan, C. S.; Subramanian, R.; Lira, C. T.; Orth, M. Adsorption and Desorption of Carbon Dioxide onto and from Activated Carbon at High Pressures. *Ind. Eng. Chem. Res.* **1997**, *36*, 2808−2815.

(42) Fitzgerald, J. E.; Sudibandriyo, M.; Pan, Z.; Robinson, R. L.; Gasem, K. A. M. Modeling the Adsorption of Pure Gases on Coals with the SLD Model. *Carbon* **2003**, *41*, 2203−2216.

(43) Liu, Y.; Hou, J.; Wang, C. Absolute Adsorption of CH4 on Shale with the Simplified Local-Density Theory. *SPE J.* **2020**, *25*, 212−225.

(44) Aranovich, G. L.; Donohue, M. D. Theory of Multilayer Adsorption with Correct Critical Behavior. *Langmuir* **2003**, *19*, 3822−3829.

(45) Merey, S.; Sinayuc, C. Analysis of Carbon Dioxide Sequestration in Shale Gas Reservoirs by Using Experimental Adsorption Data and Adsorption Models. *J. Nat. Gas Sci. Eng.* **2016**, *36*, 1087−1105.

(46) Pang, Y. .; Soliman, M. Y.; Deng, H. .; Emadi, H. Analysis of Effective Porosity and Effective Permeability in Shale-Gas Reservoirs With Consideration of Gas Adsorption and Stress Effects. *SPE J.* **2017**, *22*, 1739−1759.

(47) McKee, C. R.; Bumb, A. C.; Koenig, R. A. Stress-Dependent Permeability and Porosity of Coal and Other Geologic Formations. *SPE Form. Eval.* **1988**, *3*, 81−91.

(48) Chen, T.; Feng, X.-T.; Pan, Z. Experimental Study of Swelling of Organic Rich Shale in Methane. *Int. J. Coal Geol.* **2015**, *150−151*, 64−73.

(49) Wu, T.; Zhao, H.; Tesson, S.; Firoozabadi, A. Absolute Adsorption of Light Hydrocarbons and Carbon Dioxide in Shale Rock and Isolated Kerogen. *Fuel* **2019**, *235*, 855−867.

(50) Gensterblum, Y.; Merkel, A.; Busch, A.; Krooss, B. M. High-Pressure CH4 and CO2 Sorption Isotherms as a Function of Coal Maturity and the Influence of Moisture. *Int. J. Coal Geol.* **2013**, *118*, 45−57.

(51) Chen, M.; Kang, Y.; Zhang, T.; Li, X.; Wu, K.; Chen, Z. Methane Adsorption Behavior on Shale Matrix at In-Situ Pressure and Temperature Conditions: Measurement and Modeling. *Fuel* **2018**, *228*, 39−49.